Dual-band superposition induced broadband terahertz linear-to-circular polarization converter

Xiao-Fei Zang,[1,2] Su-Ji Liu,[1] Han-Hong Gong,[1] Yajun Wang,[3] and Yi-Ming Zhu[1,2,*]

[1]Terahertz Technology Innovation Research Institute, and Shanghai Key Lab of Modern Optical System, University of Shanghai for Science and Technology, No.516 JunGong Road, Shanghai 200093, China
[2]China Terahertz Science Cooperative Innovation Center, Chengdu 610054, China
[3]North Electro-Optics Group Co,. LTD, Dian Zi San Lu Road, No. 9, Yanta District, Xi'an 710065, China
*Corresponding author: ymzhu@usst.edu.cn

A reflective broadband terahertz (THz) linear-to-circular (LTC) polarization converter based on a single-layer ultra-thin metasurface is designed and experimentally demonstrated. Two different-size rectangular ultrathin metasurface micro-structures are proposed to realize such a broadband THz LTC polarization converter with bandwidth ranging from 0.832 to 1.036 THz. The phase delay between two orthogonal resonance modes is –90° ± 5°. These qualities are realized mainly by combining two separated LTC polarization conversion frequencies and the benefit of the coupling between two different-size rectangles. The calculated results indicate that the bandwidth of the LTC polarization converter is controlled via the dimensions and period of the structure. This kind of ultrathin broadband THz polarization converter can be widely applied into wireless communication, imaging, and detection, and can widen the path to designing novel functional THz devices. © 2018 Optical Society of America

1. INTRODUCTION

Polarization converters, functional devices, have attracted much attention in recent years due to their abilities to manipulate the polarization states of electromagnetic waves. Conventional polarization converters, which are based on birefringent effects, are always determined by certain materials, including crystals [1,2] and polymers [3]. However, the intrinsic defects of these converters, i.e., limited available materials, large size, and narrow bandwidth, seriously restrict their applications, especially in the terahertz (THz) regime.

Metamaterials, which are artificial electromagnetic media consisting of periodic subwavelength metal-based micro-structures, have been proposed and provide a novel way to realize ultrathin, broadband, and miniaturized polarization converters. Many kinds of single-band [4–11], multi-band [12–15], one-way [16], and tunable [17] linear polarization converters have been realized via metamaterials technology. Furthermore, highly efficient and broadband linear polarization converters were achieved by virtue of multi-frequency superposition [18–27] or partial symmetry structures [28]. In addition to linear polarization converters, linear-to-circular (LTC) polarization converters have also attracted considerable attention owing to their potential applications in polarization manipulation, imaging, and biological detection. Broadband circular

polarization converters were reported originally based on three-dimensional helical metamaterials [29,30]. The presented LTC polarization converters were realized with a variety of asymmetric structures, i.e., split ring slot apertures [31,32], subwavelength nanoslits [33], cross-shaped apertures [34–37], elliptical patch nanoantennas [38], elliptical gratings [39], and L-shaped holes [40], where two orthogonal resonance modes with equal amplitudes and ±90° phase delay were excited at a certain frequency, leading to LTC polarization conversion. However, an asymmetric structure is in response to a single frequency, resulting in narrowband polarization conversion. Therefore, a type of metasurface that consists of two anisotropic V-shaped antenna subunits was proposed [41], but the conversion efficiency was limited because of the low efficiency of anomalous refraction. Meanwhile, many other types of high-efficiency and wideband LTC polarization converters were reported, such as L-shaped [42] and multi-layer stacked metallic wire-grid-based [43,44] broadband LTC. However, the broadband characteristic of L-shaped broadband LTC suffered from dispersion compensation of the dielectric spacing layer. For the multi-layer design, it is crucial to integrate two separated metasurface to avoid inter-layer coupling, and more or less increase the complexity of device fabrication.

Here, we propose a broadband LTC polarization converter based on a single-layer and reflective ultrathin metasurface consisting of two different-size rectangular arrays. Each of the arrays can be considered a single-band LTC polarization converter at a certain resonance frequency, and the broadband characteristic is formed by the superposition of these two separated LTC polarization conversion resonance frequencies with optimized structure parameters. In other words, apart from the two resonance frequencies, broadband LTC conversion is realized via resonance coupling between these two different-size rectangles, which is quite different from the above dispersion-compensation-based LTC polarization converters. When compared with multi-layer broadband LTC polarization converters, the broadband single-layer LTC polarization converter proposed in this paper precisely takes advantage of the coupling between two different-size rectangles rather than avoiding the coupling between different layers ([43,44]). Numerical simulation and experimental results show that the LTC conversion efficiency is about 70% over a broad frequency range (more than 0.2 THz). We also find that the bandwidth of the device is sensitive to dimensions of these two rectangular patterns. Our approaches in achieving a broadband LTC polarization converter based on a dual-band superposition mechanism may open a new window for designing LTC polarization converters and future practical applications in many research fields, such as imaging, detection and wireless communication.

2. RESULTS AND DISCUSSION

As we all know, circular polarization of a light beam represents a polarization state, where at each point, the electric field of the wave has a constant magnitude, but its direction rotates with time at a steady rate in a plane perpendicular to the direction of the wave. The electric vector of the circular polarized light has two orthogonal components (E_x and E_y) with equal amplitude and phase delay of $\pm\pi/2$. Therefore, we should optimize our structure to obtain the orthogonal reflected electric fields (E_x and E_y) with the nearest equivalent amplitudes and phase delay nearby $\pm\pi/2$. In this work (for numerical simulations), the phase delay between the two orthogonal reflected electric fields (E_x and E_y) is in the range of –85° to –95° (–90° $\pm$ 5°) with ellipticity less than –0.99 (–1 $\leq$ ellipticity $\leq$ – 0.99).

The schematic of such a LTC polarization converter composed of two different-size rectangle arrays coating on one side of the polyimide (PI) film (with gold substrate in the backside), is shown in Fig. 1(a). The corresponding structure parameters are $h_1 = 49$ μm, $l_1 = 56.8$ μm, $h_2 = 78$ μm, $l_2 = 74.9$ μm, $P_x = 117$ μm, $P_y = 234$ μm, $d = 25$ μm, $g = 53.5$ μm, $g_1 = 34$ μm, $g_2 = 19$ μm, and the thickness of the pattern and substrate is 200 nm. When the incident THz wave is polarized at $\theta = 45°$ [see Fig. 1(b)], each of these two rectangles excite two orthogonal resonance modes with equal amplitudes and quadrature phase at two separated frequencies. These two resonance frequencies can be combined into a broadband LTC polarization by optimizing the structure parameters. The scanning electron microscope (SEM) image of the fabricated sample is shown in Fig. 2(a). We fabricated the polarization converter based on the traditional photolithography and magnetron sputtering coating. First, the substrate
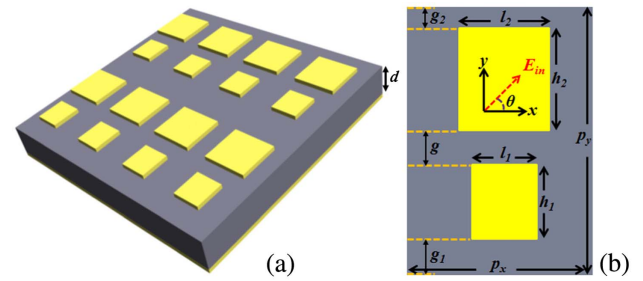

Fig. 1. (a) Schematic of the broadband THz polarization converter. (b) The corresponding unit cell. The normal incident THz wave is polarized at $\theta = 45°$ toward the x axis.
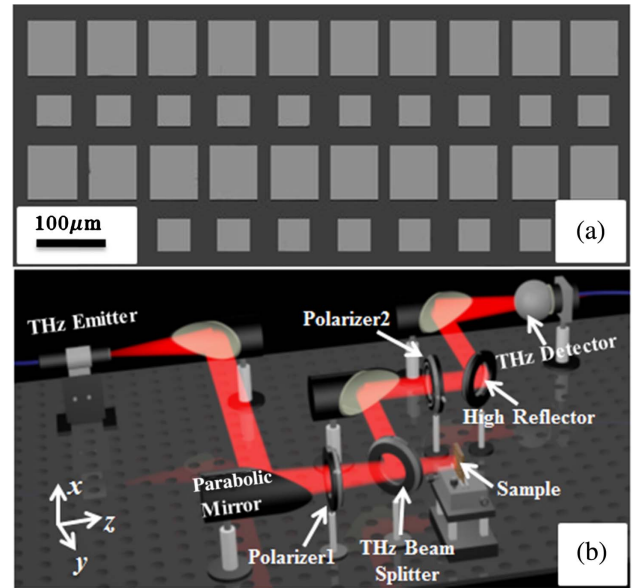

Fig. 2. (a) SEM of the fabricated structure. (b) Experimental setup.

was realized by the metal coating (by magnetron sputtering) on one side of the PI film. Then, an AZP4620 photoresist layer was spin-coated on the other side of the PI film, and we utilized the mask for exposure processing. After metal coating and ultrasonic stripping, the layer of gold rectangle array was formed. In our simulation, the permittivity of the PI is $\varepsilon_{pi} = 3.5 + 0.035i$, and the electrical conductivity of gold is 4.561×10^7 S/m. The calculated reflection coefficients and phase delay are shown in Figs. 3(a) and 3(c). At 0.856 THz [the left green dashed line in Fig. 3(a)], reflection coefficient of 0.88 with a phase delay around –90° is presented, resulting in a right-handed circularly polarized (RHCP) THz wave. By combining two polarization conversion frequencies with optimized structure parameters, a broadband circular polarized wave ranging from 0.832 to 1.036 THz is realized. Meanwhile, if the incident THz wave is polarized at $\theta = 135°$ to the x axis, a broadband of left-handed circularly polarized (LHCP) wave will be achieved.

The reflection spectra are measured by THz time-domain spectroscopy (THz-TDS) under reflection mode, as shown
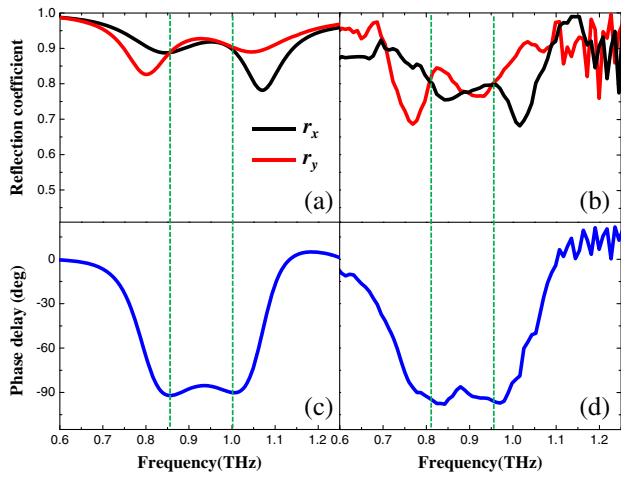
Fig. 3. Simulated and measured results of the broadband THz LTC polarization converter: the reflection coefficients of (a) simulations and (b) measurements; phase delay between two orthogonal components of (c) simulations and (d) measurements.

in Fig. 2(b) (experimental setup). A THz linear polarizer is located in front of each of the THz beam splitter and the detector. The first polarizer (Polarizer 1) is introduced to get a linearly polarized incident THz wave, while the other polarizer (Polarizer 2) is applied to measure polarization states of the output THz wave. The measured reflection coefficients and phase delay are shown in Figs. 3(b) and 3(d), respectively. Two orthogonal resonance modes with equal reflection coefficient and phase difference of –90° are excited at 0.810 THz [the left green dashed line of Fig. 3(b)], which demonstrates that the incident THz wave with a linear polarization state is converted into a RHCP THz wave. In the same way, RHCP with reflection coefficient of 0.80 is also achieved at 0.952 THz [the right green dashed line of Fig. 3(d)]. Therefore, we can realize a broadband LTC polarization converter by combining two conversion frequencies with optimized structure parameters. The corresponding simulation results are shown in Figs. 3(a) and 3(c). Both the calculated and measured spectra show good agreement, except for slight difference in resonance frequencies, due to fabrication error.

To verify polarization states of the output THz waves, we introduce the Stokes parameters as

$$S_0 = |\tilde{r}_x|^2 + |\tilde{r}_y|^2,$$
$$S_1 = |\tilde{r}_x|^2 - |\tilde{r}_y|^2,$$
$$S_2 = 2|\tilde{r}_x||\tilde{r}_y|\cos(\varphi_d),$$
$$S_3 = 2|\tilde{r}_x||\tilde{r}_y|\sin(\varphi_d), \qquad (1)$$

where S_0 is the field intensity of output THz waves. S_1 is the linearly polarized component along the x axis, S_2 is a linearly polarized component in the direction of 45°, and S_3 is a circularly polarized component. φ_d is the phase difference between the two orthogonal components ($\varphi_d = \varphi_{E_y} - \varphi_{E_x}$, and E_y and E_x are the two vertical components). Based on Eq. (1), we can obtain the ellipticity χ defined as $\chi = S_3/S_0$.
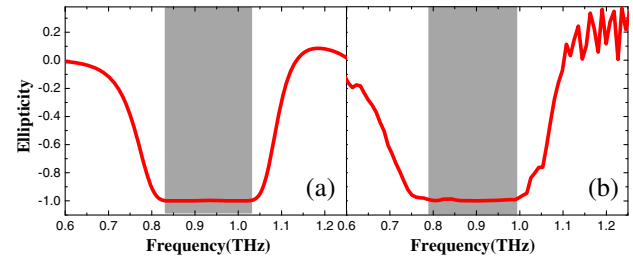

Fig. 4. (a) Simulated and (b) measured ellipticity.

When $\chi = 1$, the reflected THz wave is perfect LHCP light, while the reflected THz wave is perfect RHCP light for $\chi = -1$. According to the simulation result, the ellipticity is around –1 between 0.832 and 1.036 THz [shown in the gray zone of Fig. 4(a)], resulting in broadband THz LTC polarization conversion. The experimentally measured result, as depicted in Fig. 4(b), also demonstrates the characteristic of RHCP light ranging from 0.787 to 0.99 THz. The theoretical results show good agreement with experimental results, except for a slight mismatch due to the fabrication errors. More intuitively, the wavefront trajectory curve is adopted to denote the polarization state of the reflected wave. Here, we introduce the vector wave equation as

$$\frac{x^2}{a^2} + \frac{y^2}{b^2} - 2\frac{xy\,\cos(\varphi_d)}{ab} = \sin^2(\varphi_d), \qquad (2)$$

where a and b are the reflection amplitudes along the x direction and y direction, respectively. According to Eq. (2), the wavefront trajectory curves of the reflected wave are given at some frequencies, such as 0.84 THz, 0.9 THz, 0.96 THz, and 1.02 THz (Fig. 5). The wavefront trajectory curves at these four frequencies are circles, indicating circularly polarized light of the reflected waves.
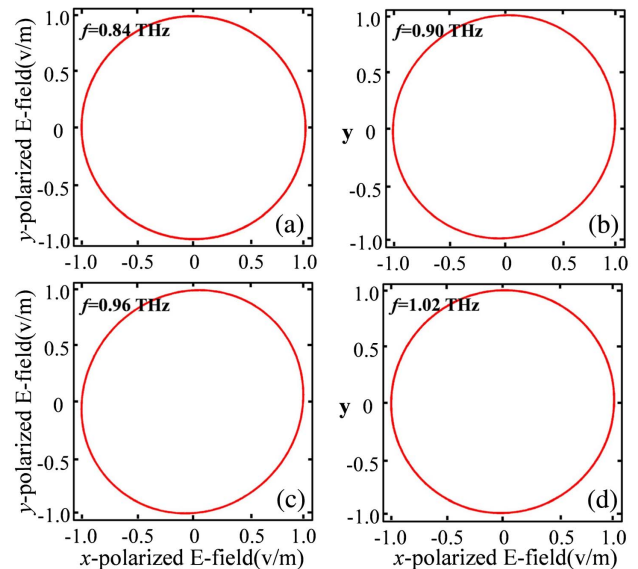

Fig. 5. Normalized wavefront trajectory curves of the reflected waves at 0.84, 0.9, 0.96, and 1.02 THz.

Now, we discuss the physical mechanism of such a broadband THz polarization converter. Electric field distributions of our designed device are shown in Fig. 6. At 0.856 THz, the excited electric field is located at the vertical bounds of the large rectangle for horizontally polarized incident THz waves [Fig. 6 (a_1)], and in turn, it is focused onto the vertical bounds of the large rectangle for perpendicularly polarized incident THz waves [Fig. 6(a_2)]. In this situation, the reflection coefficients of the orthogonal electric fields are equal, and the phase delay between them is –90° [see Figs. 3(a) and 3(c)]. That is, LTC polarization conversion at 0.856 THz is mainly attributed to the resonance of the large rectangle. Meanwhile, at 1.0 THz, the two orthogonally incident linearly polarized THz beams are mainly confined in two orthogonal bounds of the small rectangle, which means that the LTC polarization conversion at 1.0 THz relies on the resonance of the small rectangle [see Figs. 6(c_1) and 6(c_2)]. At the intermediate frequency, i.e., 0.936 THz, both the large and small rectangles are excited with phase delay of –90° and the nearest equivalent of amplitudes between these two orthogonal components, demonstrating the effect of LTC polarization conversion [as shown in Figs. 6(b_1), 6(b_2), and 3]. The electric field distribution shown in Fig. 6 indicates that the broadband characteristic of our LTC polarization converter is achieved by combining two LTC polarization conversion frequencies with benefit of dual-band superposition between two size-different rectangles.

Since the broadband properties of the designed LTC converter are determined mainly by two different-size rectangles, we now investigate the variation of phase delay and ellipticity

of the LTC converter with different dimensions of the two rectangular patterns. Figure 7 shows the phase delay and ellipticity of the LTC converter under the modulation of h_1. In fact, the LTC conversion is generated from the anisotropic of the rectangular patterns. The anisotropic is derived from the unequal effective length of each rectangle in both the x and y axes, i.e., the effective indices of the rectangle in the x and y axes are not equal, thus a 90° phase shift (with equal reflection coefficients) at a certain frequency is achieved for a special aspect ratio of the rectangle. For example, when $h_1 = 49$ µm and $l_1 = 56.8$ µm, perfect LTC conversion is achieved at $f = 1.0$ THz. When the structure parameter h_1 is diverging from the optimized value ($h_1 = 49$ µm), the phase delay between the orthogonal electric fields also deviates from –90° as shown in Fig. 7(a), leading to imperfect LTC conversion at $f = 1.0$ THz. It should be noted that the amplitudes of two orthogonal electric fields have changed very little for different-dimension modulations of h_1 (not shown here). Figure 7(b) shows that peaks appear at the high-frequency regime (nearby $f = 1.0$ THz) due to imperfect LTC conversion. Figures 7(c)–7(g) show the wavefront trajectories with different values of h_1 at $f = 1.0$ THz. They all manifest as elliptical polarized wavefronts, except for $h_1 = 49$ µm. In a word, for the imperfect structure parameter of h_1 ($h_1 \neq 49$ µm), the bandwidth of the LTC converter is less than 0.2 THz [see Fig. 7(b)]. In contrast, the phase delay in the low-frequency regime ($f = 0.856$ THz) is fixed, which demonstrates that the phase delay is modulated by changing dimensions of the small rectangle in the high frequency regime. In other words, the LTC conversion in the high-frequency regime is decided by
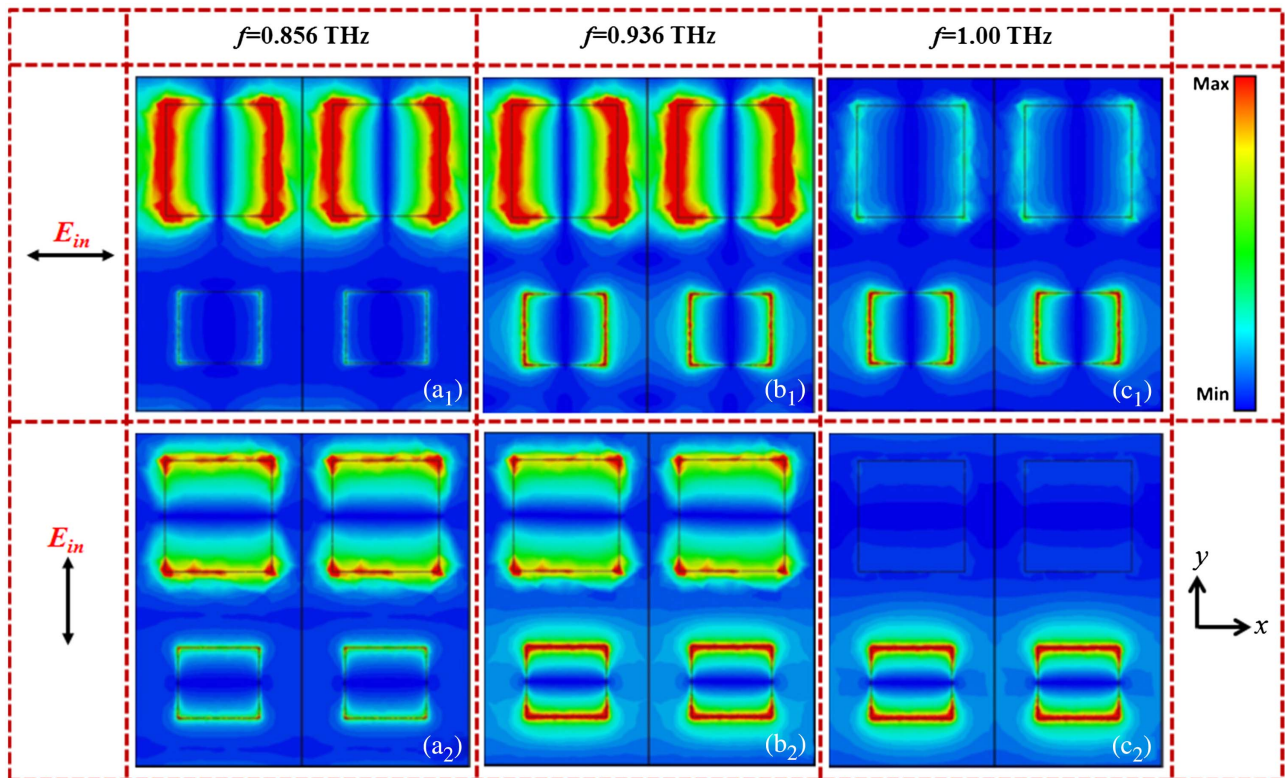

Fig. 6. Electric field distribution for two orthogonal polarized waves at (a) 0.856 THz, (b) 0.936 THz, and (c) 1.0 THz.
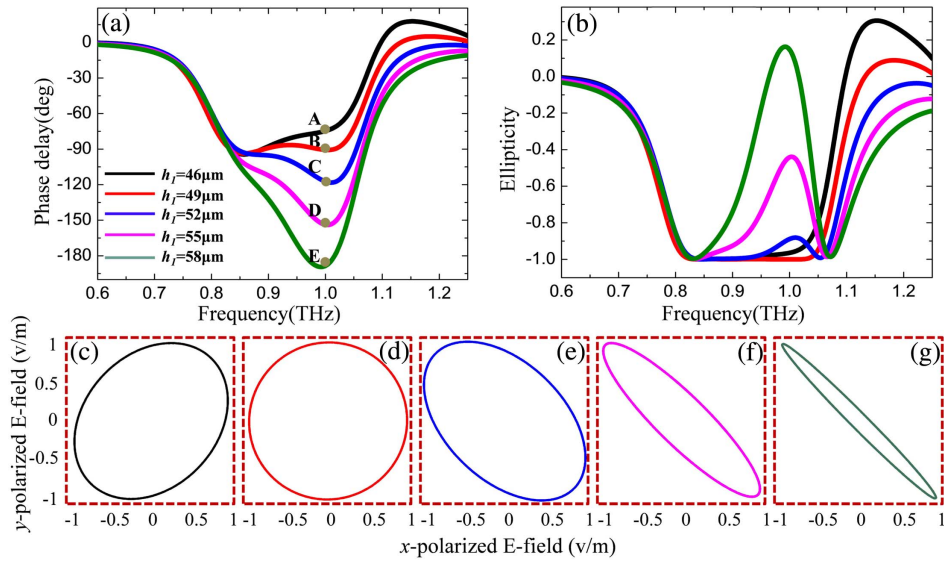
Fig. 7.   (a) Phase delay and (b) ellipticity for different h_1. (c)–(g) The normalized wavefront trajectories for different h_1 at $f = 1.0$ THz with the corresponding phase delay [between these two orthogonal electric fields (E_x and E_y)] shown at points A, B, C, D, and E in (a).

the small rectangle. A similar phenomenon is also found by adjusting the structure parameter l_1.

Figure 8 illustrates the corresponding results by modulating structure parameter h_2. Phase delay in the low-frequency regime, i.e., $f = 0.856$ THz, is manipulated by changing the size of h_2. Similarly, phase delay induced by the large rectangle is also deflected from –90°, and h_2 gradually changes from 72 to 84 μm ($h_2 \neq 78$ μm), as shown in Fig. 8(a). In this situation, the peaks appear in the low-frequency regime ($f = 0.856$ THz), reducing the bandwidth of the LTC conversion [see Fig. 8(b)]. The wavefront trajectories for different h_2 are shown in Figs. 8(c)–8(g), demonstrating imperfect LTC conversion for $h_2 \neq 78$ μm.

Figure 9 illustrates the phase delay and corresponding ellipticity of the LTC converter with different thicknesses of the polyimide film. The phase delay is modulated by structure parameter d, as shown in Fig. 9(a). This can be explained qualitatively as follows. The reflected THz waves can be divided into two parts: one part is reflected directly from the surface of the rectangular patterns, while the other part is reflected from the substrate that is sensitive to the thickness of the PI film. Therefore, when structure parameter d diverges from the optimized value ($d = 25$ μm), the phase delay between the orthogonal electric fields also deviates from –90° as shown in Fig. 9(a), resulting in a bandwidth-reduced LTC [see the corresponding ellipticity in Fig. 9(b)].
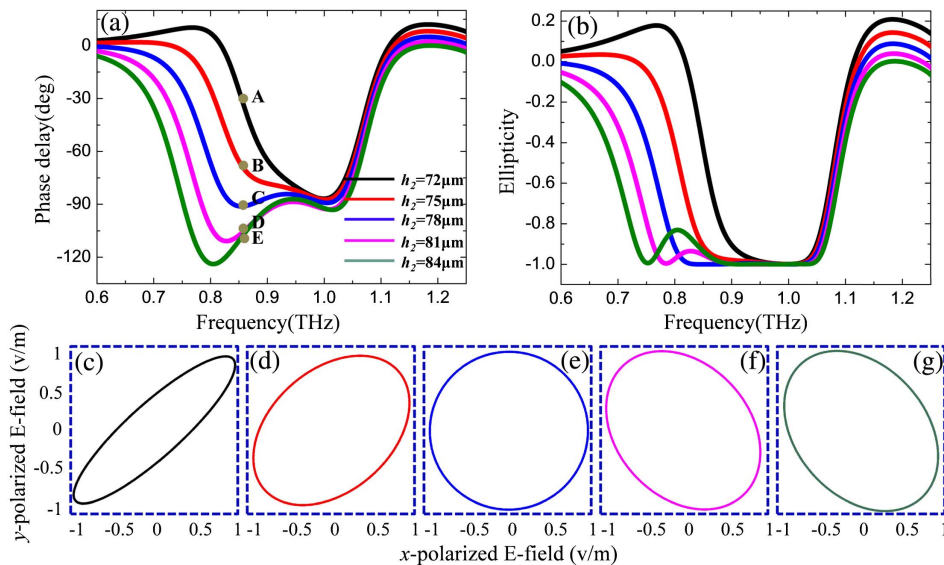

Fig. 8.   (a) Phase delay and (b) ellipticity for different h_2. (c)–(g) The normalized wavefront trajectories for different h_2 at $f = 0.856$ THz with the corresponding phase delay [between these two orthogonal electric fields (E_x and E_y)] shown at points A, B, C, D, and E in (a).
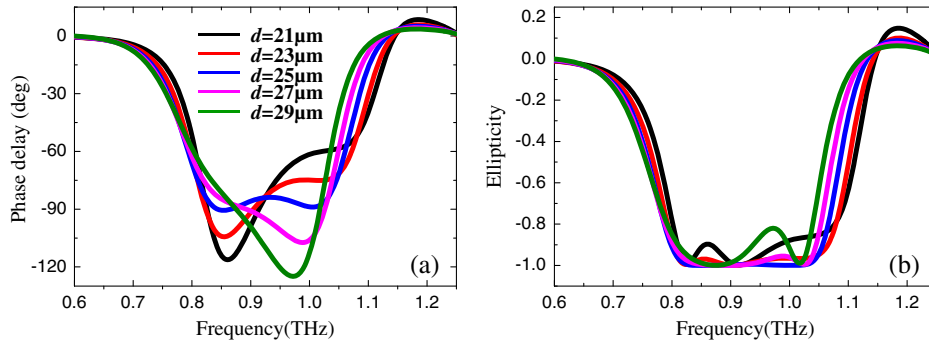
Fig. 9.   Phase delay (a) and ellipticity (b) for different thickness of polyimide film.
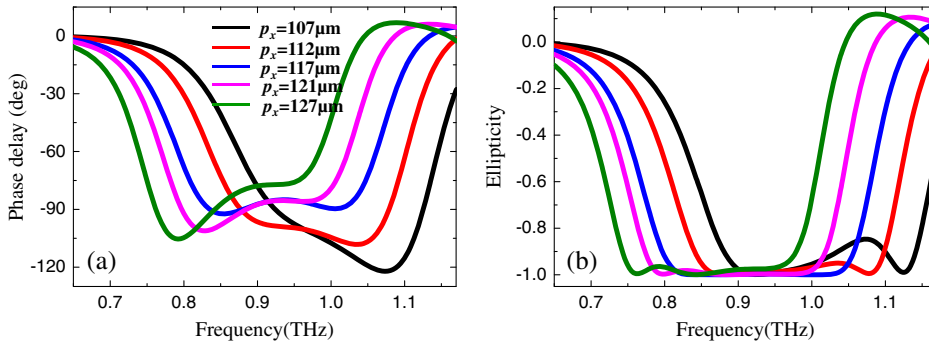

Fig. 10.   (a) Phase delay and (b) ellipticity for different periods with size-variational rectangular patterns. $L_1 = 0.49P_x$, $h_1 = 0.42P_x$, $L_2 = 0.64P_x$, $h_2 = 0.67P_x$, and $P_y = 2P_x$.

We also numerically demonstrate the polarization transformation performance for the model with large and small sizes. Here, the dimension (size) of the rectangular patterns is unitarily changed with the variation of the period. When the period (p_x) is changed gradually from 107 to 127 μm, the size of rectangular patterns also becomes larger and larger. Therefore, the resonant frequency is shifted to the low-frequency regime, as shown in Fig. 10(b). In the meantime, the phase delay between the orthogonal electric fields is also deviates from –90° for unmatched pattern size, period, and gap between the rectangular patterns [as shown in Fig. 10(a)],

leading to an imperfect broadband LTC [also see the ellipticity in Fig. 10(b)].

Finally, we discuss the polarization transformation property of the designed LTC device with different periods and a fixed-size rectangular pattern. The centers of the big and small rectangles are located in (0, $p_y/4$) and (0, $–p_y/4$), respectively. When the period is increased, the gap distance between these two rectangles is also enhanced, but the dimension (size) of the rectangles is fixed. When the period (p_x) is gradually changed from 107 to 127 μm, there are two dips near 0.85 and 1.03 THz, corresponding to the two resonance frequencies
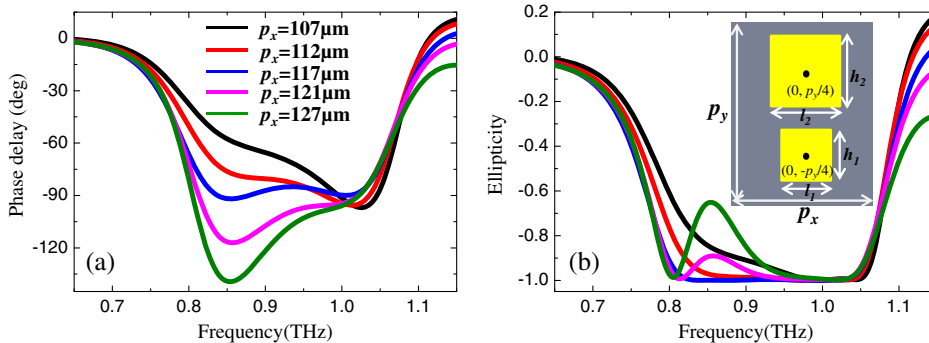

Fig. 11.   (a) Phase delay and (b) ellipticity for different period with size-fixed rectangular patterns. $L_1 = 56.8$ μm, $h_1 = 49$ μm, $L_2 = 74.9$ μm, $h_2 = 78$ μm, and $P_y = 2P_x$. Inset is the schematic of the THz polarization converter. The centers of the large and small rectangles are located in (0, $p_y/4$) and (0, $–p_y/4$), respectively. The black dots in the inset represent the centers of the rectangles.

of the large and small rectangles, respectively. Here, these two rectangles are fixed, and, thus, the resonance frequencies are invariable. However, when the gap distance diverges from the perfect value ($g = 53.5$ μm), the phase delay also deviates from −90° (due to the mismatch of the gap distance), as shown in Fig. 11(a), leading to a bandwidth-decreased LTC converter [see the ellipticity in Fig. 11(b)].

3. CONCLUSION

In summary, we experimentally demonstrate a single-layer broadband THz LTC polarization converter. Such a device can convert a linearly polarized wave to a circularly polarized wave in a broad frequency ranging from 0.832 to 1.036 THz. The broadband characteristic of our polarization converters is attributed to the combination of two separated LTC polarization conversion frequencies and the benefit of the coupling interaction between two different-sized rectangles. LTC conversion efficiency of over 70% can be achieved for ellipticity around −1. Moreover, the calculated phase delay and ellipticity in different dimensions of two rectangular patterns demonstrates that the broadband performance is affected by the aspect ratio of each rectangle and the period of the structure. Such an ultrathin dual-band superposition-induced broadband LTC converter will have great potential applications in the area of wireless communication, imaging, and detection, and open a new way to design novel functional THz devices.

REFERENCES

1. J. B. Masson and G. Gallot, "Terahertz achromatic quarter-wave plate," Opt. Lett. **31**, 265–267 (2006).
2. A. Saha, K. Bhattacharya, and A. K. Chakraborty, "Achromatic quarter-wave plate using crystalline quartz," Appl. Opt. **51**, 1976–1980 (2012).
3. M. Scheller, C. Jördens, and M. Koch, "Terahertz form birefringence," Opt. Express **18**, 10137–10142 (2010).
4. T. Li, S. M. Wang, J. X. Cao, H. Liu, and S. N. Zhu, "Cavity-involved plasmonic metamaterial for optical polarization conversion," Appl. Phys. Lett. **97**, 261113 (2010).
5. Z. Marcet, H. B. Chan, D. W. Carr, J. E. Bower, R. A. Cirelli, and F. Klemens, "A half wave retarder made of bilayer subwavelength metallic apertures," Appl. Phys. Lett. **98**, 151107 (2011).
6. Y. J. Chiang and T. J. Yen, "A composite-metamaterial-based terahertz-wave polarization rotator with an ultrathin thickness, an excellent conversion ratio, and enhanced transmission," Appl. Phys. Lett. **102**, 011129 (2013).
7. S. Wu, Z. Zhang, Y. Zhang, K. Zhang, L. Zhou, and X. Zhang, "Enhanced rotation of the polarization of a light beam transmitted through a silver film with an array of perforated s-shaped holes," Phys. Rev. Lett. **110**, 207401 (2013).
8. H. Cheng, S. Chen, P. Yu, J. Li, B. Xie, and Z. Li, "Dynamically tunable broadband mid-infrared cross polarization converter based on graphene metamaterial," Appl. Phys. Lett. **103**, 223102 (2013).
9. Z. Li, M. Mutlu, and E. Ozbay, "Highly asymmetric transmission of linearly polarized waves realized with a multilayered structure including chiral metamaterials," J. Phys. D **47**, 075107 (2014).
10. C. Huang, Q. Wang, X. Yin, Y. Zhang, J. Li, and Y. Zhu, "Break through the limitation of Malus' law with plasmonic polarizers," Adv. Opt. Mater. **2**, 723–728 (2015).
11. C. Pfeiffer, C. Zhang, V. Ray, L. J. Guo, and A. Grbic, "Polarization rotation with ultra-thin bianisotropic metasurfaces," Optica **3**, 427–432 (2016).
12. J. Shi, X. Liu, S. Yu, T. Lv, Z. Zhu, and H. F. Ma, "Dual-band asymmetric transmission of linear polarization in bilayered chiral metamaterial," Appl. Phys. Lett. **102**, 191905 (2013).
13. H. Shi, A. Zhang, S. Zheng, J. Li, and Y. Jiang, "Dual-band polarization angle independent 90° polarization rotator using twisted electric-field-coupled resonators," Appl. Phys. Lett. **104**, 034102 (2014).
14. J. Tang, Z. Xiao, K. Xu, X. Ma, D. Liu, and Z. Wang, "Cross polarization conversion based on a new chiral spiral slot structure in THz region," Opt. Quantum. Electron. **48**, 1–11 (2016).
15. J. Woo, S. Hussain, and J. Jang, "A terahertz in-line polarization converter based on through-via connected double layer slot structures," Sci. Rep. **7**, 42952 (2017).
16. F. Fan, S. T. Xu, X. H. Wang, and S. J. Chang, "Teraherta polarization converter and one-way transmission based on double-layer magneto-plasmonics of magnetized InSb," Opt. Express **24**, 26431–26443 (2016).
17. B. Vasic, D. C. Zografopoulos, G. Isic, R. Beccherelli, and R. Gajic, "Electrically tunable terahertz polarization converter based on over-coupled metal-isolator-metal metamaterials infiltrated with liquid crystals," Nanotechnology **28**, 124002 (2017).
18. N. K. Grady, J. E. Heyes, D. R. Chowdhury, Y. Zeng, M. T. Reiten, A. K. Azad, A. Taylor, D. Dalvit, and H. T. Chen, "Terahertz metamaterials for linear polarization conversion and anomalous refraction," Science **340**, 1304–1307 (2013).
19. L. Cong, W. Cao, X. Zhang, Z. Tian, J. Gu, and R. Singh, "A perfect metamaterial polarization rotator," Appl. Phys. Lett. **103**, 171107 (2013).
20. Q. Levesque, M. Makhsiyan, P. Bouchon, F. Pardo, J. Jaeck, and N. Bardou, "Plasmonic planar antenna for wideband and efficient linear polarization conversion," Appl. Phys. Lett. **104**, 111105 (2014).
21. D. Y. Liu, M. H. Li, X. M. Zhai, L. F. Yao, and J. F. Dong, "Enhanced asymmetric transmission due to Fabry-Perot-like cavity," Opt. Express **22**, 11707–11712 (2014).
22. Y. Z. Cheng, W. Withayachumnankul, A. Upadhyay, D. Headland, Y. Nie, and R. Z. Gong, "Ultrabroadband reflective polarization convertor for terahertz waves," Appl. Phys. Lett. **105**, 181111 (2014).
23. K. Song, Y. Liu, C. Luo, and X. Zhao, "High-efficiency broadband and multiband cross-polarization conversion using chiral metamaterial," J. Phys. D **47**, 505104 (2014).
24. R. W. Peng, R. H. Fan, Y. Zhou, S. C. Jiang, X. Xiong, and X. R. Huang, "Freely-tunable broadband polarization rotator for terahertz waves," Adv. Mater. **27**, 1201–1206 (2015).
25. Z. Li, S. Chen, W. Liu, H. Cheng, Z. Liu, and J. Li, "High performance broadband asymmetric polarization conversion due to polarization-dependent reflection," Plasmonics **10**, 1703–1711 (2015).
26. Z. Song, J. Zhu, C. Zhu, Z. Yu, and Q. Liu, "Broadband cross polarization converter with unity efficiency for terahertz waves based on anisotropic dielectric meta-reflectarrays," Mater. Lett. **159**, 269–272 (2015).
27. C. P. Huang, "Efficient and broadband polarization conversion with the coupled metasurfaces," Opt. Express **23**, 32015–32024 (2015).
28. H. Cheng, J. Tian, J. Li, P. Yu, S. Chen, and W. Liu, "Realization of broadband cross-polarization conversion in transmission mode in the terahertz region using a single-layer metasurface," Opt. Lett. **40**, 3185–3188 (2015).
29. J. K. Gansel, M. Thiel, M. S. Rill, M. Decker, K. Bade, and V. Saile, "Gold helix photonic metamaterial as broadband circular polarizer," Science **325**, 1513–1515 (2009).
30. Y. Zhao, M. A. Belkin, and A. Alù, "Twisted optical metamaterials for planarized ultrathin broadband circular polarizers," Nat. Commun. **3**, 870 (2012).

31. M. Euler, V. Fusco, R. Cahill, and R. Dickie, "325 GHz single layer sub-millimeter wave FSS based split slot ring linear to circular polarization convertor," IEEE Trans. Antennas Propag. **58**, 2457–2459 (2010).

32. D. C. Wang, L. C. Zhang, Y. D. Gong, L. Jian, T. Venkatesan, C. W. Qiu, and M. H. Hong, "Multiband switchable quarter-wave plates via phase-change metasurface," IEEE Photon. J. **8**, 5500308 (2016).

33. E. H. Khoo, E. P. Li, and K. B. Crozier, "Plasmonic wave plate based on subwavelength nanoslits," Opt. Lett. **36**, 2498–2500 (2011).

34. A. Roberts and L. Lin, "Plasmonic quarter-wave plate," Opt. Lett. **37**, 1820–1822 (2012).

35. D. C. Wang, Y. H. Gu, Y. D. Gong, C. W. Qiu, and M. H. Hong, "An ultrathin terahertz quarter-wave plate using planar Babinet-inverted metasurface," Opt. Express **23**, 11114–11122 (2015).

36. D. C. Wang, L. C. Zhang, Y. H. Gu, M. Q. Mehmood, Y. D. Gong, A. Srivastava, L. Jian, T. Venkatesan, C. W. Qiu, and M. H. Hong, "Switchable ultrathin quarter-wave plate in terahertz using active phase-change metasurface," Sci. Rep. **5**, 15020 (2015).

37. F. Wang, A. Chakrabarty, F. Minkowski, K. Sun, and Q. H. Wei, "Polarization conversion with elliptical patch nanoantennas," Appl. Phys. Lett. **101**, 023101 (2012).

38. Y. Gorodetski, E. Lombard, A. Drezet, C. Genet, and T. W. Ebbesen, "A perfect plasmonic quarter-wave plate," Appl. Phys. Lett. **101**, 201103 (2012).

39. B. Yang, W. M. Ye, X. D. Yuan, Z. H. Zhu, and C. Zeng, "Design of ultrathin plasmonic quarter-wave plate based on period coupling," Opt. Lett. **38**, 679–681 (2013).

40. N. Yu, F. Aieta, P. Genevet, M. A. Kats, Z. Gaburro, and F. Capasso, "A broadband, background-free quarter-wave plate based on plasmonic metasurfaces," Nano Lett. **12**, 6328–6333 (2012).

41. S. Jiang, "Controlling the polarization state of light with a dispersion-free metastructure," Phys. Rev. X **4**, 021026 (2014).

42. H. F. Ma, G. Z. Wang, G. S. Kong, and T. J. Cui, "Broadband circular and linear polarization conversions realized by thin birefringent reflective metasurfaces," Opt. Mater. Express **4**, 1717–1724 (2014).

43. L. Cong, N. Xu, J. Gu, R. Singh, J. Han, and W. Zhang, "Highly flexible broadband terahertz metamaterial quarter-wave plate," Laser Photon. Rev. **8**, 626–632 (2014).

44. L. Cong, N. Xu, J. Han, W. Zhang, and R. Singh, "A tunable dispersion-free terahertz metadevice with Pancharatnam-Berry-phase-enabled modulation and polarization control," Adv. Mater. **27**, 6630–6636 (2015).